ChemComm

COMMUNICATION

View Article Online
View Journal

Cite this: DOI: 10.1039/d6cc01855f

Received 26th March 2026,
Accepted 11th May 2026

DOI: 10.1039/d6cc01855f

rsc.li/chemcomm

Dynamic structural evolution of soft colloidal monolayers under uniaxial compression

Vahan Abgarjan,[a] Arkadiy Simonov,[b] Keumkyung Kuk *[ac] and Matthias Karg[ad]

Real-time small-angle light scattering of microgels at the air/water interface during Langmuir trough compression and expansion cycles reveals a reversible 30° reorientation of the hexagonal lattice, mediated by a metastable rectangular phase.

Studies of colloids at fluid interfaces holds significance across technical applications (*e.g.*, emulsion stabilization,[1,2] material engineering[3–5]) as well as fundamental research (*e.g.*, self-assembly,[6–8] colloidal interactions[9,10]). Langmuir troughs (LTs) are commonly used to fabricate 2D structured materials and investigate assembly and phase behaviors.[11–14] The typical approach involves adsorbing the colloids of interest at fluid interfaces followed by controlled lateral compression using two barriers (changeable length l and fixed width w, Fig. 1A) after a certain equilibration time while measuring surface pressure, Π. During this compression process, soft and deformable colloids such as microgels exhibit a spectrum of interparticle distances, in contrast to their rigid counterparts. In addition, the potential for forming non-hexagonal self-assembled structures (due to the soft interaction potential,[15] *e.g.*, core–shell (CS) structured microgels with hydrodynamic diameter, D_h, Fig. 1B) has captured the interest of a broad scientific community and has been extensively explored in recent years.[11,14]

Recent works brought attention to the importance of *in situ* monitoring of soft colloids during such interfacial assembly processes. Using small-angle light scattering (SALS)[16] and fluorescence microscopy combined with a LT,[17,18] *in situ* microstructures were shown to differ from those obtained *ex situ* after Langmuir–Blodgett deposition, evidencing transfer-induced structural changes.[19] Furthermore, despite maintaining near-hexagonal order, uniaxial LT compression was found to induce anisotropy in the microstructure even at low speeds.[20] Similar findings were reported in different systems, evidenced by an orientation-dependent Π, *e.g.*, silica nanoparticles,[21] carbon nanotubes,[22] poly(*N*-isopropylacrylamide) (PNIPAM) microgels,[23] and proteins.[24] This suggests deformation and relaxation colloid monolayers of during uniaxial compression is more intricate than previously assumed. To fill this knowledge gap, fast and non-invasive *in situ* measurements are required.

Here we move beyond near-equilibrium assembly and examine the dynamic, out-of-equilibrium lattice changes of soft colloidal monolayers at the air/water interface (deformed due to surface tension with diameter, D_i, at the interface, Fig. 1C) during compression and expansion cycles using LT-SALS. This approach allows real-time structural monitoring over mm^2-scale areas at higher compression and expansion speeds, information inaccessible to real-space microscopy.

Using seeded precipitation polymerization, we synthesized CS microgels with silica cores and soft, deformable PNIPAM shells. The cores had mean diameter of 340 nm measured by transmission electron microscopy (JEOL JEM-2100 Plus). We used a nominal crosslinker density of 5.2 mol% for the shells.

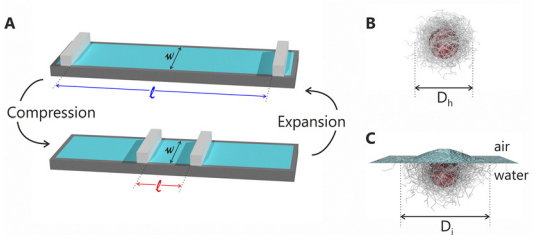

Fig. 1 (A) Uniaxial compression/expansion in a Langmuir trough (length l, width w) at the air/water interface. (B) CS microgel in bulk (hydrodynamic diameter D_h) and (C) adsorbed at the air/water interface (interfacial diameter D_i). $D_i > D_h$ owing to lateral stretching of the shell by the large interfacial tension.

[a] *Institut für Physikalische Chemie I: Kolloide und Nanooptik, Heinrich-Heine-Universität Düsseldorf, Universitätsstr. 1, 40225, Düsseldorf, Germany*
[b] *Disordered Materials, Department of Materials, ETH Zürich, Vladimir-Prelog-Weg 5, 8093, Zürich, Switzerland*
[c] *Laboratory for Soft Materials and Interfaces, Department of Materials, ETH Zürich, Vladimir-Prelog-Weg 5, 8093, Zürich, Switzerland. E-mail: keumkyung.kuk@mat.ethz.ch*
[d] *Physikalische Chemie funktionaler Polymere, Institut für Chemie, Martin-Luther-Universität Halle-Wittenberg, Von-Danckelmann-Platz 4, 06120, Halle (Saale), Germany*

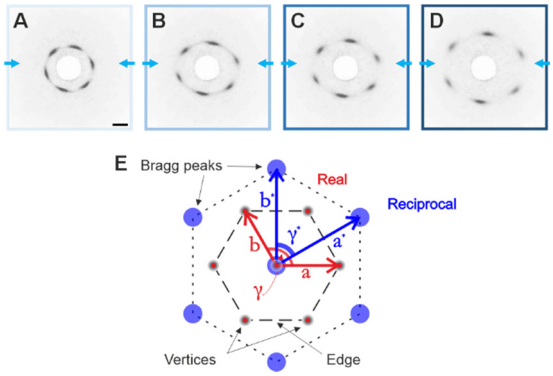

Fig. 2 (A)–(D) Diffraction patterns of a CS monolayer during slow conventional compression at Π = 23.2, 26.6, 27.6 and 29.6 mN m^{-1}. Blue arrows indicate the compression direction (scale bar 10 μm). (E) Real-space lattice vectors *a*, *b* and angle γ (red), with the corresponding reciprocal lattice vectors *a**, *b** and angle γ* (blue).

This resulted in microgels with overall hydrodynamic diameter, D_h of 791 nm (swollen state) measured by dynamic light scattering (Zetasizer Nano S, Malvern Panalytical). Detailed synthesis and purification protocols are described elsewhere.[25] The microgels in ethanol were spread onto the air/water interface in the Langmuir trough and left to equilibrate for at least 30 minutes. CS microgels are known to adsorb strongly to liquid interfaces.[14] Compression and expansion experiments were performed in a Langmuir trough (KSV NIMA, Biolin Scientific) equipped with a microscopy window in the bottom plate. Diffraction patterns were recorded by LT-SALS in real time. Setup specifications and measurement protocols are detailed elsewhere.[16,20]

Fig. 2 shows representative diffraction patterns from monolayers that self-assembled from monodisperse CS microgels during conventional uniaxial compression. The total reduction in interface area with a slow compression speed of 1 mm min^{-1} corresponds to 43% of the initial area. The captured diffraction patterns, initially in blue (l_{Laser} = 405 nm) on a dark background, were converted to grayscale and inverted using ImageJ.[26] Additionally, the patterns were rotated to align the compression direction horizontally for reasons of clarity and visibility. The diffraction patterns in Fig. 2A–D show pronounced Bragg peaks with a six-fold symmetry that is related to the hexagonal packing (p6mm symmetry) of the CS microgels in the monolayer. The peaks shift to higher angles, *i.e.*, the radial positions of the peak centers increase as Π increases (measured Πs: (A) 23.2, (B) 26.6, (C) 27.6, and (D) 29.6 mN m^{-1}), indicating that the interparticle distance decreases with compression (calculated assuming that the microstructure is hexagonally assembled and its strain is the same in all directions: (A) 963 ± 76, (B) 785 ± 75, (C) 687 ± 52, and (D) 600 ± 41 nm).The diffraction patterns become increasingly stretched along the compression direction with increasing compression, *i.e.* reduction in area. This anisotropy (aspect ratio, fitted with an ellipse: (A) 1.06, (B) 1.16, (C) 1.16, and (D) 1.15) indicates that the interparticle distance along the compression axis decreases in real space relative to the orthogonal direction (width direction of the trough, *w*, as depicted in Fig. 1A). The corresponding compression isotherm and interparticle distance as a function of surface pressure as well as normalized trough area, can be found in the SI, in Fig. S1 and Table S1. For clarity, we will refer to samples with stretched six Bragg peaks as hexagonal lattices throughout this article if they retain six peaks, although strictly speaking they no longer exhibit six-fold rotational symmetry. For numerous microgel-assembled monolayers, the initial lattice orientation appears to be random. However, as compression proceeds, the lattice tends to reorient in such a way that two vertices of the hexagon in real space align with the compression direction. Fig. 2E illustrates the relationship between the real and reciprocal lattice of a hexagonal structure in terms of lattice vectors and the angles between them. The blue circles represent the reciprocal lattice points (Bragg peaks) resembling the diffraction pattern captured in Fig. 2D, while the red circles and vectors represent the corresponding real-space lattice.

This preference for lattice orientation is somewhat counter-intuitive, as simple geometric considerations would suggest that compression along the edges would allow for more efficient packing through particle sliding. However, the observed preference for vertex alignment suggests that non-linear effects and collective particle interactions dominate over simple packing considerations. Fig. 3 simulates vertex-vertex (A)–(C) and edge-edge compression (D)–(F) of the hexagon. Compression along the vertices causes the microgels at the vertices to come into contact with the central microgel earlier on ("hard direction") while leaving empty spaces between the rows of microgels. In contrast, compression along the edges (D) and (E) allows the two microgels at the ends of the edges to slide between the microgels in neighboring rows ("soft direction") and thus higher compression state. As compression proceeds in a soft direction, the microgel array undergoes a transitional phase before returning to hexagonal symmetry with its lattice orientation shifted by 30 degrees during the process. This behavior has not been observed in conventional Langmuir compression at low speeds, likely due to the relatively fast relaxation and rearrangement of microgels under such conditions. When the compression speed is high, the strain on the monolayer is likely more pronounced per unit time while relaxation remains slow. These dynamic rearrangements can reveal metastable phases and yield insight into interparticle potentials and transition states.[27]

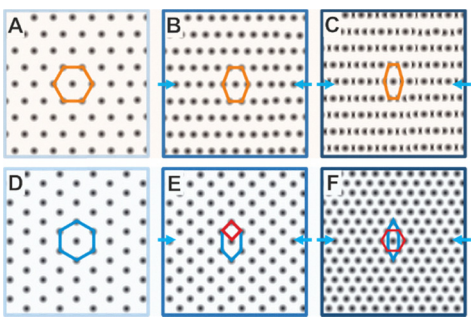

Fig. 3 Simulated compression of a hexagonal microgel lattice. (A)–(C) Vertex–vertex ("hard direction"): vertex microgels meet the central microgel, leaving empty spaces between rows. (D)–(F) Edge–edge ("soft direction"): edge microgels slide between neighboring rows.

In slow uniaxial compression, the locally measured Π is generally assumed to represent the overall compression state of the monolayer. This assumption breaks down at high compression speeds, which can cause uneven stress distribution, anisotropic strain, and a local structural gradient,[20,22,28] one must therefore be cautious when comparing Π measured at different and/or high speeds (see Fig. S2 for slow *vs.* fast interparticle distance hysteresis). Fig. 4 shows a rapid expansion-compression cycle of the pre-assembled CS monolayer recorded *via* LT-SALS at 27 mm min^{-1} compression speed. The full Video S1 of this rapid expansion-compression cycle can be viewed in SI. The diffraction pattern in Fig. 4A shows the microgel monolayer from Fig. 2D after being further compressed to Π of 30 mN m^{-1}, reducing the trough area from 43% to 31%. The system was then allowed to equilibrate for 30 minutes before structural investigation. After the equilibration time, the calculated interparticle distance remains at 607 $\pm$ 20 nm, comparable to the situation in Fig. 2D (600 $\pm$ 41 nm) despite further reducing the area, indicating that the microgels relax over time. The microstructure relaxation, accompanied by an increase in interparticle distance, becomes more evident when the monolayer is subjected to perturbation, such as in oscillating barrier experiments, where the two barriers oscillate sinusoidally around a target position. This relaxation behavior of the microgel monolayer can be observed in Video S2, captured during an oscillating barrier experiment (frequency 200 mHz, area change relative to the starting area 2%). Further evidence of this relaxation is the accompanying change in the aspect ratio of the diffraction pattern, which decreases from 1.15 in Fig. 2D to 1.02 in Fig. 4A.

Fig. 4(B)–(D) show the evolution of the diffraction pattern during the rapid expansion at a barrier speed of 27 mm min^{-1}, which features a smooth, near 30° rotation of the Bragg peaks, with a pair of peaks eventually aligning with the compression direction. This indicates that the lattice orientation of the monolayer at the measuring point (at the center of the trough) rotates from a "hard" to a "soft direction" as the monolayer expands. Additionally, the pattern becomes elongated perpendicular to the expansion direction, reflecting that the average interparticle distance along the expansion direction is larger than that along the orthogonal direction. This behavior contrasts with the observations during slow compression. The measured aspect ratios are (B) 1.34, (C) 1.27, and (D) 1.17 (with the trough area 76%), which are significantly higher than those observed during slower compression, highlighting the pronounced anisotropy induced by the faster expansion process. Upon recompression, as the trough area decreases to 42% (Fig. 4E–H), the elongation direction shifts by 90° (Fig. 4E), signifying that the average interparticle distance along the compression direction is shorter than that along the orthogonal direction. Then the intriguing 30° shift of the lattice orientation ("soft" to "hard" direction, Fig. 4G and H) unfolds through a dynamic metastable phase transition (Fig. 4F) with a rectangular (p2mm like) symmetry.

Fig. 5 depicts real space microstructures reconstructed from the diffraction patterns in Fig. 4. Each panel includes an inset on the top right showing the corresponding Fast Fourier Transform (FFT) of the reconstructed microstructure, which agrees with the diffraction patterns shown in Fig. 4. The Jupyter Notebook code used for the FFT generation can be found in SI. The reconstruction of real space microstructure was done using reciprocal lattice parameters acquired from the diffraction patterns: reciprocal lattice vectors (a^* and b^*) and the angle γ^* between them (see Fig. 2E), to calculate the real space lattice vectors (a and b) and their corresponding angle γ, where $\gamma = 180° - \gamma^*$. The magnitudes of the real space vectors were determined based on the inverse proportionality between the reciprocal and real lattices ($a \propto 1/a^*$, $b \propto 1/b^*$). Operation of stretching and rotation (using an angle between the compression/expansion axis and a^*, see Fig. S3) were applied independently to account for lattice deformations. The microstructure in Fig. 5A exhibits an initial hexagonal arrangement, with a uniform distribution of particles (representing microgels at the air/water interface) and minimal deformation. As the expansion proceeds (Fig. 5B–D), the particles along the expansion direction are further away from each other, decreasing the particle number density along the expansion direction. The simultaneous decrease in particle number density along the orthogonal direction (fixed width, w of the trough) suggests that the microgels also exhibit vertical mobility during the fast barrier movement. Fig. 5D–H illustrate the behavior of the microgel monolayer during compression, showing a dynamic reorganization of the particles similar to what was observed in the expansion cycle, *i.e.*, the reversible and adaptive nature of the microgel lattice. Moreover, the 30° shift of lattice orientation and the rectangular metastable phase captured as diffraction patterns in Fig. 4E–H, and the corresponding reconstructed

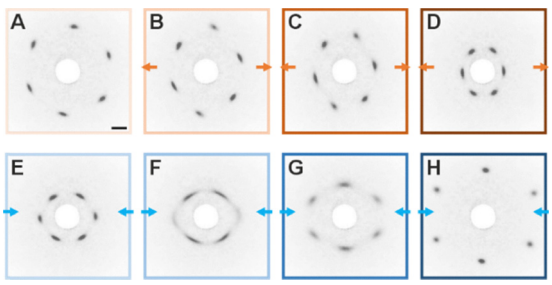

Fig. 4 Rapid expansion–compression cycle of a CS monolayer. (A) 30 min after compression to ≈ 30 mN m^{-1} (from Fig. 2D). (B)–(D) Expansion (orange) and (E)–(H) recompression (blue) at barrier speed 27 mm min^{-1} (scale bar 10 μm).

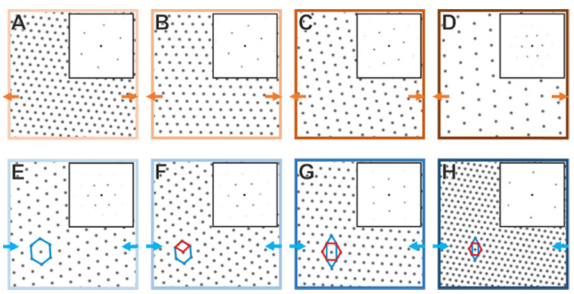

Fig. 5 Real-space microstructure reconstructed from the Fig. 4 diffraction patterns, during expansion (A–D, orange) and recompression (E–H, blue). Top-right insets show the corresponding FFTs.

microstructure in Fig. 5D–G bear a strong resemblance to the simulated FFTs and hexagonal array lateral compression in the ''soft direction'' in Fig. 3D–F *via* a transitional phase with a rectangular symmetry. Across all simulations, microgels deform by sliding into neighboring rows, even when vertical rearrangement occurs. It is worth noting that in Fig. 5F, despite the symmetry of the diffraction patterns resembling a rectangular lattice due to the fading pair of Bragg peaks along the compression axis, the reconstruction of the microstructure was based on hexagonal symmetry, as the diffraction pattern still exhibits six Bragg peaks. Consequently, the reconstruction accuracy in this case may be lower than the others, where the Bragg peaks are more distinct and well-defined.

Stopping the compression at the metastable rectangular phase results in immediate (matter of seconds) relaxation of the monolayer back into hexagonal symmetry, although reproducible over multiple compression and expansion cycles, see Fig. S4 and Table S2. Neither the conventional Langmuir–Blodgett deposition at a fixed Π nor the Langmuir-Schäfer deposition method was able to capture the induced metastable phase or the anisotropy of the microgel monolayers at the air/water interface on a substrate. This is likely due to the rearrangement of microgels during the drying process in the thin water film on the solid substrate, driven by immersion capillary forces.[19] Knowing the hexagonal lattice orientation and the stretching directions enables control over the deposition process, allowing for either linear or rectangular orders to be achieved on a solid substrate. Using our CS microgels, we successfully obtained non-hexagonal orders *via* reverse Langmuir–Blodgett deposition, see Fig. S5 and S6. Similar to the method described in ref. 29, the monolayer is deposited on hydrophobically surface-modified substrates from air to the subphase, *i.e.*, water. Hydrophobic surface modification enhances microgel–substrate adhesion, preventing the rearrangement in the thin water film[30] that otherwise occurs upon transfer onto a like-charged hydrophilic substrate.[19] Several non-hexagonal orders of such monolayers on solid substrates (*ex situ*) were also reported for similarly sized coreless microgels,[8] hairy particles[31] and binary systems.[32,33]

In this work, we have studied the dynamic structural changes in CS microgel monolayers at air/water interfaces under uniaxial compression and expansion, captured in real time by small-angle light scattering. We demonstrate a reproducible 30° shift in hexagonal lattice orientation, mediated by a metastable rectangular phase. We attribute this behavior to the softness and deformability of microgels, which allow them to act simultaneously as individual building blocks and as an elastic sheet. This work captures the rich dynamic landscape accessible only through *in situ* observation. We hope this study inspires further investigations into the effects of confinement geometry (*e.g.*, trough shape) on resulting microstructures, and the role of various shell morphologies.

K. K.: conceptualization, writing (original draft). M. K.: supervision, funding acquisition. V. A.: methodology. A. S.: formal analysis. All authors contributed to the review and editing.

Conflicts of interest

There are no conflicts to declare.

Data availability

All data generated or analyzed during this study are included in this published article (and its supplementary information (SI) files). Supplementary information includes the calculated inter-particle distance as a function of surface pressure as well as normalized trough area, the same metastable rectangular phase captured in other microgel systems and their *ex situ* arrays. Video S1 (d6cc01855f3) shows the fast expansion-compression cycle depicted in Fig. 4A. Video S2 (d6cc01855f4) shows microgel monolayer relaxation duing an oscillating barrier experiment. See DOI: https://doi.org/10.1039/d6cc01855f.

Acknowledgements

A Part of the research has been funded by Deutsche Forschungsgemeinschaft (DFG, KA3880/6-1). K. K. acknowledges Prof. Lucio Isa (ETH Zürich) for a helpful discussion and for enabling fruitful collaboration with A.S.

References

1 F. Bresme and M. Oettel, *J. Phys.: Condens. Matter*, 2007, **19**, 413101.
2 E. Vignati, R. Piazza and T. P. Lockhart, *Langmuir*, 2003, **19**, 6650–6656.
3 M. He, J. P. Gales, É. Ducrot, Z. Gong, G.-R. Yi, S. Sacanna and D. J. Pine, *Nature*, 2020, **585**, 524–529.
4 I. T. Chen, E. Schappell, X. Zhang and C.-H. Chang, *Microsyst. Nanoeng.*, 2020, **6**, 22.
5 Y. Fang, B. M. Phillips, K. Askar, B. Choi, P. Jiang and B. Jiang, *J. Mater. Chem. C*, 2013, **1**, 6031.
6 D. M. Balazs, T. A. Dunbar, D.-M. Smilgies and T. Hanrath, *Langmuir*, 2020, **36**, 6106–6115.
7 S. Mičky, M. Bodík, M. Mičetić, F. Fetzer, M. Strienz, V. Held, M. Jergel, A. Schnepf, F. Schreiber and P. Šiffalovič, *Langmuir*, 2022, **38**, 14850–14856.
8 M. A. Fernandez-Rodriguez, M.-N. Antonopoulou and L. Isa, *Soft Matter*, 2021, **17**, 335–340.
9 M. J. Bergman, N. Gnan, M. Obiols-Rabasa, J.-M. Meijer, L. Rovigatti, E. Zaccarelli and P. Schurtenberger, *Nat. Commun.*, 2018, **9**, 5039.
10 S. Bochenek, C. E. McNamee, M. Kappl, H.-J. Butt and W. Richtering, *Phys. Chem. Chem. Phys.*, 2021, **23**, 16754–16766.
11 D. Feller and M. Karg, *Soft Matter*, 2022, **18**, 6301–6312.
12 E. Guzmán and A. Maestro, *Polymers*, 2022, **14**, 1133.
13 S. Ciarella, M. Rey, J. Harrer, N. Holstein, M. Ickler, H. Löwen, N. Vogel and L. M. C. Janssen, *Langmuir*, 2021, **37**, 5364–5375.
14 M. Rey, M. A. Fernandez-Rodriguez, M. Karg, L. Isa and N. Vogel, *Acc. Chem. Res.*, 2020, **53**, 414–424.
15 E. A. Jagla, *Phys. Rev. E*, 1998, **58**, 1478–1486.
16 K. Kuk, V. Abgarjan, L. Gregel, Y. Zhou, V. Carrasco Fadanelli, I. Buttinoni and M. Karg, *Soft Matter*, 2023, **19**, 175–188.
17 T. Kawamoto, K. Yanagi, Y. Nishizawa, H. Minato and D. Suzuki, *Chem. Commun.*, 2023, **59**, 13289–13292.
18 A. Rubio-Andrés, D. Bastos-González and M. A. Fernandez-Rodriguez, *J. Colloid Interface Sci.*, 2025, **688**, 328–340.
19 K. Kuk, J. Ringling, K. Gräff, S. Hänsch, V. Carrasco-Fadanelli, A. A. Rudov, I. I. Potemkin, R. Von Klitzing, I. Buttinoni and M. Karg, *Adv. Sci.*, 2024, **11**, 2406977.
20 V. Abgarjan, K. Kuk, J. L. S. Garthe, T. L. Wigger and M. Karg, *Soft Matter*, 2025, **21**, 5030–5044.
21 D. Y. Zang, E. Rio, D. Langevin, B. Wei and B. P. Binks, *Eur. Phys. J. E*, 2010, **31**, 125–134.

22 S. R. Vora, B. Bognet, H. S. Patanwala, C. D. Young, S. Y. Chang, V. Daux and A. W. K. Ma, *J. Colloid Interface Sci.*, 2018, **509**, 94–101.
23 Y. S. Tein, B. R. Thompson, C. Majkrzak, B. Maranville, D. Renggli, J. Vermant and N. J. Wagner, *Rev. Sci. Instrum.*, 2022, **93**, 093903.
24 P. Cicuta and E. M. Terentjev, *Eur. Phys. J. E*, 2005, **16**, 147–158.
25 K. Kuk, L. Gregel, V. Abgarjan, C. Croonenbrock, S. Hänsch and M. Karg, *Gels*, 2022, **8**, 516.
26 C. A. Schneider, W. S. Rasband and K. W. Eliceiri, *Nat. Methods*, 2012, **9**, 671–675.
27 R. W. Perry, M. C. Holmes-Cerfon, M. P. Brenner and V. N. Manoharan, *Phys. Rev. Lett.*, 2015, **114**, 228301.
28 E. Aumaitre, D. Vella and P. Cicuta, *Soft Matter*, 2011, **7**, 2530–2537.
29 M. E. J. Hummel, C. Stelling, B. A. F. Kopera, F. A. Nutz, M. Karg, M. Retsch and S. Förster, *Langmuir*, 2019, **35**, 973–979.
30 L. H. Alvarez, A. A. Rudov, R. A. Gumerov, P. Lenssen, U. Simon, I. I. Potemkin and D. Wöll, *Phys. Chem. Chem. Phys.*, 2021, **23**, 4927–4934.
31 J. Menath, J. Eatson, R. Brilmayer, A. Andrieu-Brunsen, D. M. A. Buzza and N. Vogel, *Proc. Natl. Acad. Sci. U. S. A.*, 2021, **118**, e2113394118.
32 M. Rey, A. D. Law, D. M. A. Buzza and N. Vogel, *J. Am. Chem. Soc.*, 2017, **139**, 17464–17473.
33 F. Grillo, M. A. Fernandez-Rodriguez, M.-N. Antonopoulou, D. Gerber and L. Isa, *Nature*, 2020, **582**, 219–224.